CFD-DEM characterization and population balance modelling of a dispersive mixing process

Chemical Engineering Science 260 (2022) 117859

Contents lists available at ScienceDirect

Chemical Engineering Science

journal homepage: www.elsevier.com/locate/ces

CFD-DEM characterization and population balance modelling of a dispersive mixing process

Graziano Frungieri [a], Gianluca Boccardo [a], Antonio Buffo [a], Hossein Ali Karimi–Varzaneh [b], Marco Vanni [a]

[a] Department of Applied Science and Technology, Politecnico di Torino, Torino, Italy
[b] Continental Reifen Deutschland GmbH, Hannover, Germany

HIGHLIGHTS

- A numerical method to study dispersive mixing in an internal mixer is presented.
- CFD simulations are used to compute the flow field in an internal mixer.
- A discrete element method based on Stokesian dynamics is used to predict breakup.
- Agglomerate breakup data are used to tune a population balance model.

ARTICLE INFO

Article history:
Received 21 February 2022
Received in revised form 23 June 2022
Accepted 4 July 2022
Available online 13 July 2022

Keywords:
Dispersive mixing
Internal mixer
Breakup
Population balance equation
CFD
DEM

ABSTRACT

This work investigates the breakup dynamics of solid agglomerates in a polymer compounding operation, by using computational fluid dynamics (CFD) simulations together with discrete element method (DEM) simulations. CFD simulations are used to compute the flow field and the shear stress distribution inside a 2D section of a typical internal mixer for polymer compounding. DEM simulations are instead used to predict the mechanical response of the agglomerates and to detect the critical viscous shear stress needed to induce breakup. DEM breakup data and viscous stress distributions are correlated by a first–time passage–statistics and used to calibrate a population balance model. The work returned detailed insights into the flow field characteristics and into the dispersive mixing kinetics. The simulation strategy herein reported can be adapted to study generic solid–liquid disperse flows in which the breakup of the solid phase is found at the core of the system behaviour.

1. Introduction

Solid fillers are often used to impart improved mechanical, thermal, chemical and/or electric properties to polymer materials. In the tire industry, for instance, carbon black and silica agglomerates are often used as reinforcing fillers to reduce wear and increase the strength and longevity of the tire (Manas-Zloczower, 2012). Nanoclays are also interesting as reinforcing fillers because of their ability to enhance the mechanical properties of the compounds at a fairly low content (Shah et al., 2016; Eckel et al., 2004). Also graphene nanosheets have found application as fillers, and they were seen to be able to improve the interface thermal properties in electronic components (Tang et al., 2015; Gravelle et al., 2020), to improve the selectivity of polymer membranes (Gontarek et al., 2019), and to confer anticorrosion properties to polymer coatings (Dutta et al., 2018).

Solid fillers often exist in the form of micron-sized agglomerates of smaller primary particles, and it is commonly accepted that the optimal performance of a polymer composite can be attained only if such agglomerates are broken down to smaller entities and uniformly distributed throughout the matrix. Dispersion is often carried out in the heavy equipment traditionally used for melt mixing, and the breakup of the fillers in such equipment is caused by the flow–induced stress. This is an attractive method in terms of industrial production, as it avoids the use of solvents, it can use well-known polymer processing equipment (e.g. intermeshing or tangential internal mixers, single or twin screw extruders), and it is capable of delivering high outputs. In the past decades, the fluid dynamics of internal mixers has been investigated for different rotor designs and operative conditions, such as rotor speed ratio, fill factor and batch temperature, by using flow visualization techniques (Freakley and Patel, 1987; Min and White, 1987) or computational fluid dynamics simulations (Cheng and Manas-Zloczower,

https://doi.org/10.1016/j.ces.2022.117859
0009-2509/

1989; Cheng and Manas-Zloczower, 1990; Yang and Manas-Zloczower, 1992; Salahudeen et al., 2011; Dhakal et al., 2017; Connelly and Kokini, 2006). A kinetic model counting for the aggregation and breakup of fillers in an extrusion process has also been devised (Berzin et al., 2002), and, recently, finite volume method simulations have been used to study dispersion kinetics in static mixers (Ferrás et al., 2021).

On the filler particle scale, various approaches can be used to investigate breakup, including Lagrangian tracking (Babler et al., 2012; Marchioli and Soldati, 2015), population balance models (Marchisio et al., 2003; Vanni, 2000), stress analysis (Breuer and Khalifa, 2019), or first–principle models (Conchúir and Zaccone, 2013; Zaccone et al., 2009). However, most of these models are not able to take into account the peculiar disordered structure of agglomerates, that often presents weak points and local heterogeneities, which may play an important role in the breakup mechanism (Horwatt et al., 1992). This suggested the use of discrete element methods (DEM), which are able to take into full account the structure of the agglomerates, including the role that each primary particle plays in the transmission of stresses (Blais et al., 2019; Frungieri and Vanni, 2017; Frungieri and Vanni, 2021; Saxena et al., 2022).

Different degrees of complexity can be introduced in DEM simulations when modelling the fluid dynamics interactions between the suspending fluid and the solid particles. In the so–called free–draining approximation, each particle is assumed to experience the Stokes drag force, as if no other particle were in the flow (Eggersdorfer et al., 2010). However, the hydrodynamic screening effects are known to play a non–negligible role on the aggregate dynamics (Becker et al., 2009; Turetta and Lattuada, 2022a; Turetta and Lattuada, 2022b). These can be taken into account by geometrical considerations based on the particle exposed surface (Higashitani et al., 2001; Fanelli et al., 2006), or by the method of reflections, for instance (Gastaldi and Vanni, 2011). However, more accurate predictions are given by Stokesian dynamics (Durlofsky et al., 1987; Brady and Bossis, 1988). This method, by using a low-order expansion of the exact solution of the flow field, is able to evaluate the hydrodynamic forces acting on each particle for any possible spatial arrangement (Seto et al., 2011; Harada et al., 2006) and it has been used over the years to predict particle aggregation (Frungieri and Vanni, 2017; Frungieri et al., 2020a), agglomerate restructuring, and the breakup of soft and rigid agglomerates in both uniform shear (Vanni and Gastaldi, 2011; Vanni, 2015; Ren et al., 2015; Harshe and Lattuada, 2012) and bounded flows (Vasquez Giuliano et al., 2022).

However, established models bridging the filler and equipment scale phenomena when dealing with the investigation of a dispersive mixing process are still missing. In a previous work from our group we employed CFD simulations coupled to DEM simulations to investigate the dispersive mixing process in an internal mixer (Frungieri et al., 2020b). The work assumed the dispersing media to be a Newtonian fluid and the filler particles to be rigid isostatic agglomerates undergoing instantaneous breakup as soon as the flow–induced stress exceeded the bond strength at any monomer–monomer contact location. In the present work we improve substantially our computational model by 1. addressing breakup in a more detailed way by using DEM simulations, built upon Stokesian dynamics, that keep into account deformation, restructuring and fragment size distribution, 2. by including the effect of the non–Newtonian behaviour of the dispersing medium in the CFD simulations and 3. by finally calibrating a population balance model able to fully describe the kinetics of the fragmentation process.

The paper finally aims at presenting a procedure which, starting from a detailed characterization of a breakup process (in terms of fluid dynamics and filler agglomerate response to shear stress), finally leads to a population balance model able to promptly predict the overall breakup kinetics. The procedure, here applied to a polymer compounding dispersive mixing process, is suitable to be adopted to study any process in which the breakup phenomena of the solid disperse phase is found at the core of the system behaviour.

The paper is organized as follows: in Section 2, we introduce the relevant equations and operative conditions for the CFD-DEM simulations of the dispersive mixing process; in Section 3.1 and 3.2 the results of the flow field in the equipment and the response of the agglomerates to viscous shear forces are presented; in Section 3.3 the strategy used to infer the breakup rates from the CFD-DEM simulations and to calibrate the population balance model is reported. Concluding remarks follow in Section 4.

2. Numerical method

We assume the dispersing medium to be a non-Newtonian fluid with a shear-thinning behaviour which can be described by a power–law relationship, and the solid fillers to consist of micron-sized agglomerates of spherical primary particles kept together by van der Waals forces. We adopt computational fluid dynamics (CFD) simulations for evaluating the flow field inside the mixing equipment and discrete element method (DEM) simulations based on Stokesian dynamics for ascertaining the breakup occurrence. Given the small size of the agglomerates and the large viscosity of the medium, the particle Reynolds number and the particle Stokes number are much lower than the unity, meaning that the response of the agglomerates to changes in the flow field is fast and that the inertia of the agglomerates is negligible. As an additional consequence of the small size of the agglomerates, we can safely assume that the agglomerates experience locally along their trajectory a linear flow field, which can be fully described by the local components of the velocity gradient. In the DEM simulations, we assume breakup to be determined solely by the viscous shear stress exerted by the flow field. The main parameters of the simulations are reported in Table 1.

2.1. Computational fluid dynamics simulations

Since the study of the breakup of filler agglomerates is the main focus of this work, the motion of the polymer material along the axial direction of the internal mixer was here disregarded and 2D simulations were performed. The flow field was evaluated by isothermal unsteady simulations, run by using Ansys Fluent 20.2. The non-Newtonian behaviour of the fluid was modelled by a power–law relationship of the following kind:

$$\mu = k \cdot \dot{\gamma}^{n-1} \tag{1}$$

where $\dot{\gamma}$ is the shear rate, computed from the second invariant of the rate-of-deformation tensor $e_{ij} = 0.5 \cdot (du_i/dx_j + du_j/dx_i)$, k is the consistency index, assumed equal to $5.8 \cdot 10^4$ Pa s^n, and n is the power-law index, ranged between 0.2 and 0.8 in this work. Such

Table 1
Main parameters of the CFD-DEM simulation.

Parameter	Symbol	Value
Medium power-law consistency index	k	$5.8 \cdot 10^4$ Pa $\cdot$ s^n
Medium power-law index	n	0.2, 0.4, 0.8
Medium density	ρ	1000 kg $\cdot$ m^{-3}
Agglomerate gyration radius	R_g	0.233–1.071 μm
Monomer radius	a	100 nm
Rotor velocity	$\dot{\theta}$	3.145 rad $\cdot$ s^{-1}
Rotor tip-to-tip length	d_{tip}	0.743 m

a set of parameters falls within the typical value ranges used to describe polymer compounds. (Manas-Zloczower, 2012; Cheng and Manas-Zloczower, 1990; Salahudeen et al., 2011). The continuity and momentum transport equations read as follows:

$$\rho\frac{\partial u_i}{\partial x_i}=0,\quad \rho\frac{\partial u_i}{\partial t}+\rho\frac{\partial[u_iu_j]}{\partial x_j}=-\frac{\partial p}{\partial x_i}+\frac{\partial\sigma_{ij}}{\partial x_j} \tag{2}$$

where the u_i's are the velocity components of the flow, p is the fluid pressure and $\sigma_{ij}=-k\dot{\gamma}^{n-1}e_{ij}$ is the generalized stress tensor. In Eq. (2), one can notice that, because of the negligible inertia of the suspended agglomerates, no terms accounting for the back reaction of the particles on the flow was included.

The medium is mechanically stirred by the motion of two counter-rotating tangential rotors in a completely filled chamber. To handle the variation in time of the shape of the flow domain, a sliding mesh approach was adopted; the flow domain was therefore split in three distinct cell regions: two *rotors regions* and one *stator region* as illustrated in Fig. 1. The first ones rotate together with the rotors, while the second remains fixed. Thus, the grids slide past each other along two circular interfaces. No slip boundary conditions were imposed at the rotor and stator walls. The mesh is composed of 183680 quadrilateral cells and the region between the rotor tip and the chamber wall, which is the region where high shear forces establish, is resolved using 14 layers; this resolution was seen to be able to capture all the features of the flow field at any rheological parameter used to model the power–law behaviour of the fluid. A speed ratio of 1:1 (30 rpm: 30 rpm) for the rotors was investigated. Starting from the relative configuration of the rotors of Fig. 1, two complete periods were simulated with a time step $\Delta t=1\cdot10^{-3}$ s, corresponding to an angle spanned by the rotors per time step equal to 0.18°.

Given their negligible inertia, the motion of the agglomerates can be reduced to that of tracer particles and their equation of motion is thus the advection equation:

$$\dot{\mathbf{x}}_p(t)=\mathbf{u}\left(\mathbf{x}_p(t),t\right) \tag{3}$$

where $\mathbf{u}\left(\mathbf{x}_p(t),t\right)$ is the velocity of the flow at the tracer particle position.

In order to compute a set of tracer trajectories a tracking algorithm was used (Frungieri et al., 2020b). At each time step, seven field quantities, i.e., two velocity components u_i, four velocity gradients components du_i/dx_j, and the medium viscosity μ were evaluated at the center of each interior face and at the center of each boundary edge. A modified Shepard algorithm was used to compute the tracer particle trajectories and the time series of the shear stress they are subject to (Thacker et al., 2010). The algorithm computes a quadratic, smooth, and once continuously differentiable bivariate function, which interpolates the field data at the scattered nodes and can be then evaluated at arbitrary positions within the domain. Given the transient nature of the flow, the interpolants had to be recomputed on each instantaneous field data and the calculation scheme was therefore as follows:

1. The initial positions of the particles were chosen.
2. The interpolants of the six field quantities were computed on the instantaneous field data.

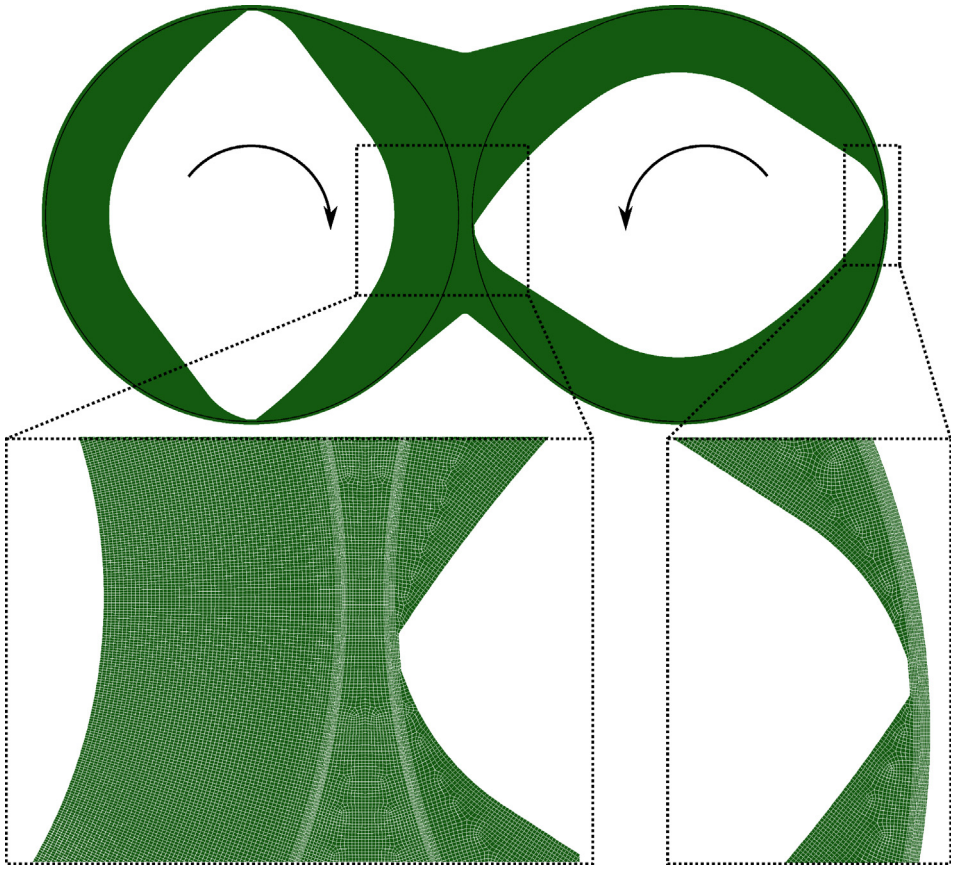

Fig. 1. Representation of the geometry of the investigated system and domain decomposition used for the sliding mesh approach, showing the two circular rotating regions and the static region. The static region includes the part of the fluid domain located between the rotors and a thin layer adjacent to the wall that surrounds the rotating regions. Mesh magnificaton of the bridge zone (bottom left) and tip zone (bottom right), showing the radial mesh used to discretize the flow domain close to the tip and the chamber wall, and the pave mesh used for discretizing the stator region in-between the rotors.

3. The seven quantities ($u_i, du_i/dx_i$ and μ) at the particle positions $\mathbf{x}_p$ were evaluated.
4. The velocity components u_i were used to obtain the new particle position by an explicit Euler integration of Eq. (3).
5. The field data was updated for the new time step.
6. Back to point 2, until particles had been tracked for two complete periods.

The algorithm has been used in a previous work and it was shown to be able to accurately track the tracer motion, preserving momentum continuity along the trajectories (Frungieri et al., 2020b).

2.2. Discrete element method simulations

Discrete element method simulations based on Stokesian dynamics were used to evaluate the critical stress needed to induce the agglomerate breakup. In using Stokesian dynamics we assume that the flow around the agglomerates is Newtonian. Indeed, due to the small size of the agglomerates, the variation of the shear rate $\dot{\gamma}$ in the surrounding fluid can be neglected and the system can be described by a constant effective viscosity $\mu = k\dot{\gamma}^{n-1}$. Stokesian dynamics, here used in its FTS (force, torque, stresslet) formulation, relying on the linearity of the Stokes equation, is able to accurately count for all the hydrodynamic interactions, including particle–fluid and fluid mediated particle–particle interactions. It operates by relating the hydrodynamic force, torque and stresslet acting on the particles to their relative velocity with respect to the underlying fluid (Durlofsky et al., 1987; Brady and Bossis, 1988).

For colloidal particles the inertial effects are generally negligible compared to the other involved forces and, consequently, the force and torque balance on each primary particle α of an agglomerate reads as:

$$\begin{cases} \mathbf{F}_{\mathrm{H}}^{(\alpha)} = -\sum \mathbf{F}_{\mathrm{p-p}}^{(\alpha)} \\ \mathbf{T}_{\mathrm{H}}^{(\alpha)} = -\sum \mathbf{T}_{\mathrm{p-p}}^{(\alpha)} \end{cases} \tag{4}$$

where $\mathbf{F}_{\mathrm{H}}$ and $\mathbf{T}_{\mathrm{H}}$ are the hydrodynamic force and torque, respectively, acting on the particle, and where the sum on the r.h.s. counts for all the forces and torques arising from the α-particle interaction with the nearby particles.

Primary particles interact via van der Waals forces, calculated as follows (Hamaker, 1937):

$$F_{\mathrm{vdW}} = \frac{A_{\mathrm{H}} \cdot a}{12 \cdot (h + \ell_0)^2} \cdot f(h) \tag{5}$$

In Eq. (5), h is the particle–particle surface distance, a the primary particle radius, A_{H} is the composite Hamaker constant for the interaction of two solids immersed in a third medium, and ℓ_0 is the minimum approach distance, assumed to be equal to 1.65 Å, and which can be thought of as the typical molecular roughness length scale of the particle surface. Finally, the term $f(h)$ takes into account the steeper decrease of the total interaction that occurs at large separation due to the retardation effect (Frungieri and Vanni, 2021).

In order to avoid compenetration among contacting particles a repulsive interaction model based on the JKR theory of contact mechanics is used. The model counts for both adhesion and deformation at the particle–particle contact plane. Its detailed description and the approach used for its implementation in the DEM simulations can be found in Frungieri and Vanni, 2021.

It is known that adhesive forces between particles give rise to a certain resistance to mutual sliding, rolling and twisting (Pantina and Furst, 2005). In order to keep into account this phenomenon, a spring force model has been introduced in our DEM simulations according to the approach proposed by Marshall (2009) and Dominik and Tielens (1997). Regarding mutual sliding, the basic idea behind this model is that, after a contact between a pair of primary particles is formed, a thought spring is initialized, whose length grows proportionally to the relative tangential velocity between the two contacting particles. Thus, the spring gives rise to a tangential restoring force F_{sld} which can be computed as:

$$F_{sld} = -k_{sld}\left(\int_{t_0}^{t} \mathbf{u}_s(\tau)d\tau\right) \cdot \mathbf{t}_s \tag{6}$$

where k_{sld} is the spring stiffness, $\mathbf{u}_s$ is the tangential projection on the contact plane of the particle–particle relative velocity, $\mathbf{t}_s$ is the slip direction, and where t_0 is the time at which the mechanical contact between particles occurred. In order to allow restructuring effect, the spring stops extending if its elongation exceeds a maximum elongation e_{sld} set equal to 3.1 nm in this work.

Similarly, when two contacting particles have different rotation rates in the normal direction (i.e. along the direction connecting their centers), a restoring twisting torque arises, which can be computed as:

$$T_{tws} = -k_{tws}\left(\int_{t_0}^{t} \Omega(\tau)d\tau\right) \cdot \mathbf{n} \tag{7}$$

where Ω is the particle–particle relative angular velocity along the normal direction $\mathbf{n}$.

A restoring torque is also present when particles are in relative rolling motion:

$$T_{rol} = -k_{rol}\left(\int_{t_0}^{t} \mathbf{u}_{\mathrm{rol}}(\tau)d\tau\right) \cdot \mathbf{t}_r \tag{8}$$

In Eq. (8), $\mathbf{u}_{rol} = -a(\omega_i - \omega_j) \times \mathbf{n}$ is the relative rolling velocity, whereas $\mathbf{t}_r = \mathbf{u}_{rol} / \mid u_{rol} \mid$ is the rolling direction. The parameters of the DEM simulations are reported in Table 2 and were estimated as detailed in the works by Marshall (2009) and Dominik and Tielens (1997) and fall within typical ranges reported for polymeric and ceramic particles in a liquid medium.

After evaluating all the particle–particle colloidal interactions, and after enforcing the force and torque balance of Eq. (4), the solution of the following linear system provides us with the angular and linear velocities of the particles:

$$\begin{bmatrix} R^{UF} & R^{\Omega F} & R^{EF} \\ R^{UT} & R^{\Omega T} & R^{ET} \\ R^{US} & R^{\Omega S} & R^{ES} \end{bmatrix} \begin{Bmatrix} \mathbf{u}^{\alpha} - \mathbf{u}^{\infty} \\ \boldsymbol{\omega}^{\alpha} - \boldsymbol{\omega}^{\infty} \\ -\mathbf{e}^{\infty} \end{Bmatrix} = -\begin{Bmatrix} \mathbf{F}^{H} \\ \mathbf{T}^{H} \\ \mathbf{S}^{H} \end{Bmatrix} \tag{9}$$

In Eq. (9), $\mathbf{u}^{\alpha}$ and $\boldsymbol{\omega}^{\alpha}$ are the linear and angular velocity of the α-th particle, respectively, $\mathbf{u}^{\infty}$ and $\boldsymbol{\omega}^{\infty}$ are the linear and angular velocity of the undisturbed fluid at the α-particle position, $\mathbf{e}^{\infty}$ is the rate-of-deformation tensor of the undisturbed fluid, and $\mathbf{S}^{H}$ is the hydrodynamic stresslet. The matrix on the l.h.s. in Eq. (9) is an $11N \times 11N$ symmetric and positive definite matrix, with N being the number of primary particles of the agglomerate. This matrix is often referred

Table 2
Main parameters of the DEM simulations.

Parameter	Symbol	Value
Primary particle radius	a	100 nm
Hamaker constant	A_H	$0.966 - 22.80 \cdot 10^{-20}$ J
Sliding resistance constant	k_{sld}	$1.595 \cdot 10^{-1}$ N/m
Rolling resistance constant	k_{rol}	$8.859 \cdot 10^{-16}$ N m rad^{-1}
Twisting resistance constant	k_{tws}	$4.429 \cdot 10^{-16}$ N m rad^{-1}
Maximum spring elongation	e_{sld}	3.1 nm
Maximum rolling displacement	e_{rol}	0.00527 rad
Maximum twisting displacement	e_{tws}	0.03927 rad
Integration time–step	dt	10^{-5} s

to as *resistance* matrix, and it depends on the particle relative positions and medium viscosity, only. The `dposv` routine from the LAPACK library was used to solve the linear system of equations of Eq. (9); the solution provided us with the primary particle velocity, from which trajectories were computed by an explicit Euler integration.

In order to predict the response of the agglomerates to the fluid shear stress, we run DEM simulations under the effect of a simple planar shear flow, whose intensity was mildly and linearly increased in time. For each DEM simulation, we detect the shear stress at which breakup occurred and the morphology and size of the generated fragments. This approach provides us with relevant information about the critical viscous stress and the fragment size distribution. Then, as it will be discussed in Section 3.3, by combining such predictions with the history of the viscous stress on the particles given by their Lagrangian tracking, through a first–time statistical analysis it is possible to calculate the frequency of breakup in the system and finally calibrate a population balance model counting for the overall breakup kinetics in the equipment.

2.3. Notes on computational costs

All the simulations were run on a workstation equipped with a Intel(R) Xeon(R) CPU E5-2630 v4 @ 2.20 GHz.

The CFD simulations were run using four processing cores exploiting the MPI parallel solver of Ansys Fluent 20.2. Each simulation required approximately 153 wall-clock minutes per physical-time second.

The interpolation code has been embedded within a tracking algorithm written in Fortran95, parallelized and run on 8 processes exploiting the MPI parallelism. Seven processes were used to interpolate the field quantities of interest (two linear velocities, four gradient components, medium viscosity) at each instantaneous tracer position. One additional master process was used to collect the data and to compute trajectories. The execution of the code for tracking 1900 tracer particles required 48.5 wall-clock minutes per physical-time second.

For our DEM simulations, the wall-clock time scales approximately with the square of the number of monomers composing the agglomerate. The simulation of an agglomerate composed of 48 monomers required 16.3 wall-clock minutes per physical-time second when executed on a single-core.

Finally, the computational cost for the solution of the population balance model was dramatically lower, accounting to few wall-clock seconds for simulating the whole solid phase population dynamics until stationary conditions were reached.

3. Results and discussion

3.1. CFD predictions

The flow field inside the mixing equipment was computed for three different values of the power–law index n of the medium (= 0.2, 0.4, 0.8). For all three cases a quite complex flow field was observed. The fluid undergoes a simple circular motion in the lobe regions, as induced by the rotation of the rotors, whereas a more complex flow pattern can be observed both in the bridge region, that is the large clearance region in-between the rotors, and in the small gap between the rotor tips and the chamber wall. The velocity flow field reported in Figs. 2a-c makes this apparent. It can be seen that the bridge region is responsible for the exchange of material between the two lobes of the mixer, as each rotor pumps the fluid in the bridge region where the flow is swept by the other rotor rotation. This mass exchange mechanism has been observed in a number of both numerical and experimental works and it can be modulated by changing the rotor speeds and design (Freakley and Patel, 1987; Salahudeen et al., 2011; Cheng and Manas-Zloczower, 1989). The region between the rotor tip and the chamber wall also presents features worth to be pointed out. Here the flow can be interpreted as the superposition of a pressure induced flow, and a drag flow, induced by the rotor rotation. As illustrated in the pressure contour plot of Fig. 2b, in front of the rotor tip, the pressure is consistently higher than in the region behind it (Freakley and Patel, 1987; Frungieri et al., 2020b). As a consequence, in the tip region the pressure flow opposes the drag flow, thus giving rise to a small recirculation vortex. However, it is apparent in Fig. 2d that the vortex dimension is strongly dependent upon the rheological features of the medium, being relatively small for the least shear thinning fluid ($n = 0.8$) and consistently larger for the most shear thinning one, where the vortex occupies almost completely the small gap between the wall and the rotor tip.

The most crucial quantities in determining the breakup of the filler agglomerates are the shear stress, which provides a measure for the local intensity of the flow-induced stress, and the mixing index, which instead provides a topological characterization of the flow field, in terms of relative importance of the elongational and rotational component of the flow. The mixing index has been computed as:

$$\lambda = \frac{\sqrt{II_{\mathbf{E}^\infty}}}{\sqrt{II_{\mathbf{E}^\infty}} + \sqrt{II_{\mathbf{\Omega}^\infty}}} \tag{10}$$

where $II_{\mathbf{\Omega}^\infty}$ is the second invariant of the vorticity tensor $\mathbf{\Omega}^\infty = 0.5\left(\nabla\mathbf{u}^\infty - \nabla\mathbf{u}^{\infty,T}\right)$ and where $II_{\mathbf{E}^\infty}$ is the second invariant of the rate-of-deformation tensor. The mixing index has a $0-1$ range, with 0 indicating a rotational motion, and 0.5 and 1 indicating pure shear and pure elongational flow, respectively. Distribution plots of the mixing index λ for three different values of the power–law index are shown in Fig. 3. In all cases, the flow field shows elongational components in the bridge region, whereas it is shear-dominated ($\lambda = 0.5$) in proximity of the chamber wall. Both the distribution of λ and its average value in the mixing chamber (0.56 for $n = 0.8$, 0.50 for $n = 0.4$, 0.41 for $n = 0.2$.) well compare with the results obtained by Cheng and Manas-Zloczower (1990) through finite element method simulations. The parameter λ is commonly considered to be important when assessing the efficiency of a flow field in inducing breakup, with a number of works that pointed out that elongational flows are more effective than shear flows (Higashitani et al., 2001; Ren et al., 2015). However such a parameter does not suffice to predict breakup, as it has to be considered together with the intensity of the viscous shear stress (Cheng and Manas-Zloczower, 1990). Therefore, we report in Fig. 4 the distribution plots of the shear stress intensity $\mu\dot{\gamma}$ computed on instantaneous field data, for the three different values of the power–law index. The figure also reports the cumulative distribution functions of the shear stress. It can be seen that the intensity of the shear stress is highly dependent upon the power-law index n. For the most shear-thinning fluid ($n = 0.2$) the maximum shear stress in the gap is around 1 MPa, but it grows as the power-law index is increased, reaching 10 MPa for the least shear thinning one ($n = 0.8$). However, it can be seen that for every n the largest values of the shear stress establish in proximity of the wall of the chamber, where $\lambda \approx 0.5$. Consequently, the largest breakup probability should be expected in the region close to the chamber wall, where the flow, as shown in Fig. 3, is largely shear–dominated.

3.2. DEM predictions

We assumed the agglomerates dispersed in the polymer medium to be composed of spherical primary particles kept together

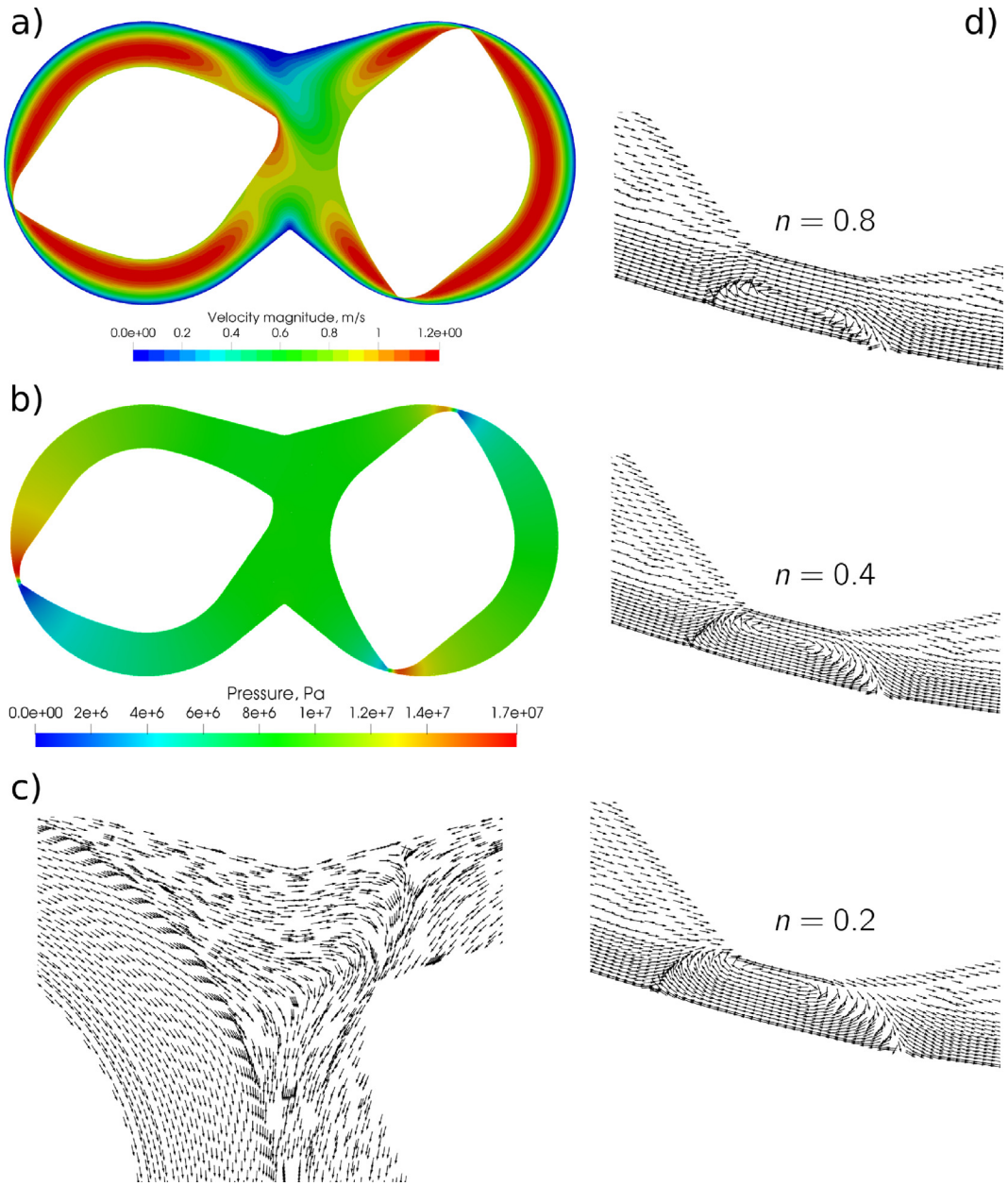

Fig. 2. Flowfield in the internal mixer as computed by the CFD simulations. (a) Velocity magnitude contour plot, (b) pressure distribution, c) velocity field by an arrow representation illustrating the mechanism of mass exchange between the lobes of the mixer. Data refer to the fluid with $n = 0.8$. d) Recirculation pattern in the gap region for varying power–law index.

by van der Waals forces, and to undergo breakup as a response to the viscous shear stress.

We generated numerically a library of agglomerates by using a cluster–cluster collision method, able to produce agglomerates with a prescribed fractal dimension, which was set to $d_f = 2.3$ in the present work (Thouy and Jullien, 1994; Filippov et al., 2000). The generation started from a population of trimers and proceeded hierarchically through the collision of equally sized agglomerates, with the generation of one single new contact at each collision event. As a consequence, the agglomerates have an isostatic structure, with each primary particle involved in two bonds only (exceptions are the terminal particles of the branches, with a single bond, and the internal particles acting as a junction between different branches, with three or more bonds). In Fig. 5 a sample of the population of agglomerates used in the simulations is shown, together with some of their relevant properties. Given the disordered structure of the agglomerates, to obtain statistically robust data, for each agglomerate size class, 10 different structures with the same number of primary particles and gyration radius were considered.

By the DEM simulations we aim at detecting the critical shear stress $\mu\dot{\gamma}$ needed to induce breakup. To this purpose in the simulations we treated the medium as a Newtonian fluid subject to an externally imposed shear rate which is progressively increased in time. Once the first breakup event was observed, the shear rate was kept constant and the simulation run until we observed the fragment size distribution to reach equilibrium, with no further breakup events detectable. For each structure we considered three different and mutually perpendicular initial orientations with respect to the flow field. The slope of the ramp was chosen by a trial and error procedure until we observed the critical shear stress to be independent of the further reduction of the slope.

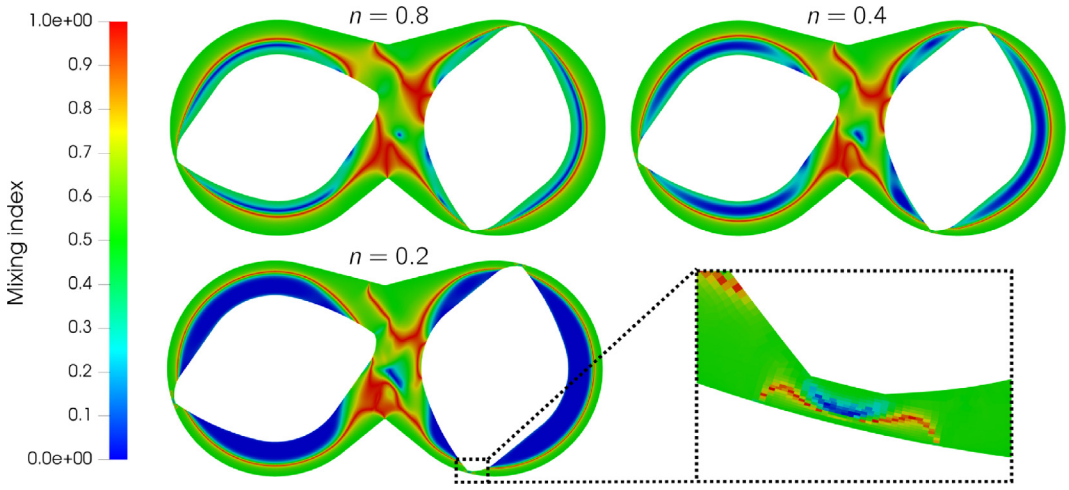

Fig. 3. Mixing index distribution for three different values of the power-law index n.

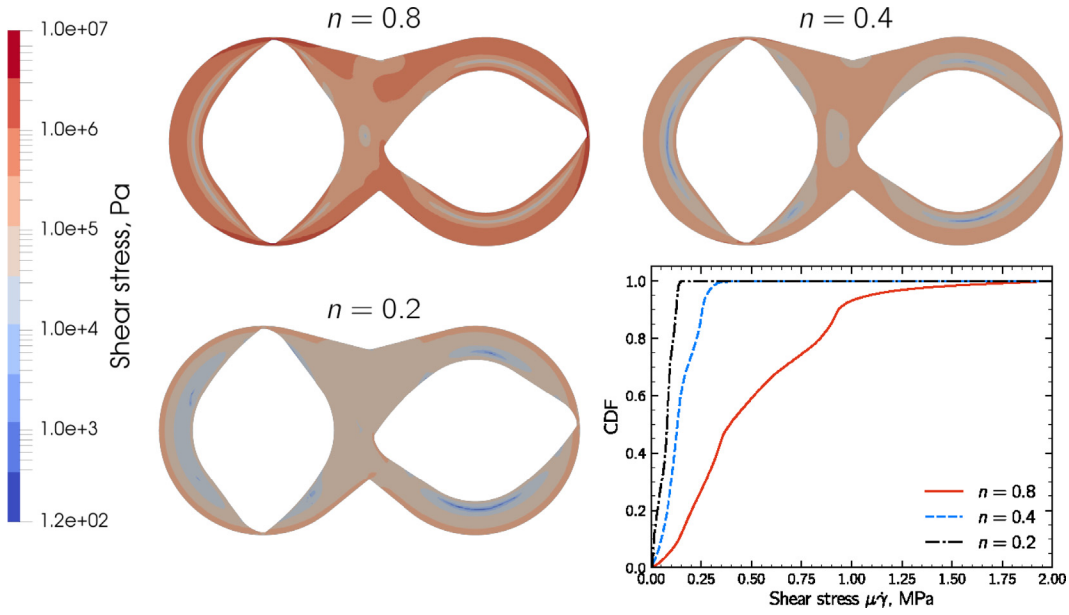

Fig. 4. Viscous stress contour plots for three different power-law index, and cumulative distribution function of the viscous shear stress intensity.

Fig. 6 reports a sequence of snapshots of a sample breakup simulation of an agglomerate made of 96 primary particles. The agglomerate rotates in the shear flow, undergoing a progressive restructuring process which leads to a compaction of its structure, and it finally undergoes breakup at the critical shear stress, generating a number of smaller fragments. To characterize the restructuring phenomenon we report in Fig. 7 the temporal evolution of an agglomerate gyration radius and average coordination number. The first is computed as the root mean square distance of the primary particles from the agglomerate center of mass, the second is computed as the average number of bonds in which primary particles are involved. It can be seen that, because of the rotational motion of the agglomerate in the shear flow, the gyration radius has an oscillatory behaviour with a sequence of minima and maxima, corresponding approximately with the maximum alignment of the agglomerate major axis with the direction of maximum tensile stress (45° with respect to flow direction) and the direction of maximum compression (−45° with respect to the flow direction), respectively. It is apparent that the gyration radius progressively reduces in time as a result of restructuring and finally the first breakup event leading to the formation of two fragments occurs. This progressive compaction phenomena is also apparent from the temporal evolution of the average coordination number. Initially the cluster has an average coordination number equally approximately to two (and corresponding to an isostatic structure), but this increases over time as a result of the generation of new internal bonds due to restructuring. This structural evolution was observed in all the agglomerates considered and led to a change of the space filling properties, which changed from a loose to a more dense packing state, with the loss of the agglomerate initial fractal features. Such an effect has to be ascribed to the onset of a relative sliding and rolling motion at the particle–particle contacts at which the sliding/rolling resistant force is exceeded by the flow induced stress.

In Fig. 8 the critical shear stress needed to observe the first breakup event is plotted as a function of the gyration radius made dimensionless by the primary particle size. Each series of data is relative to a different value of the Hamaker constant. It can be seen that as the Hamaker constant is increased, agglomerates break at a larger stress and, more remarkably,

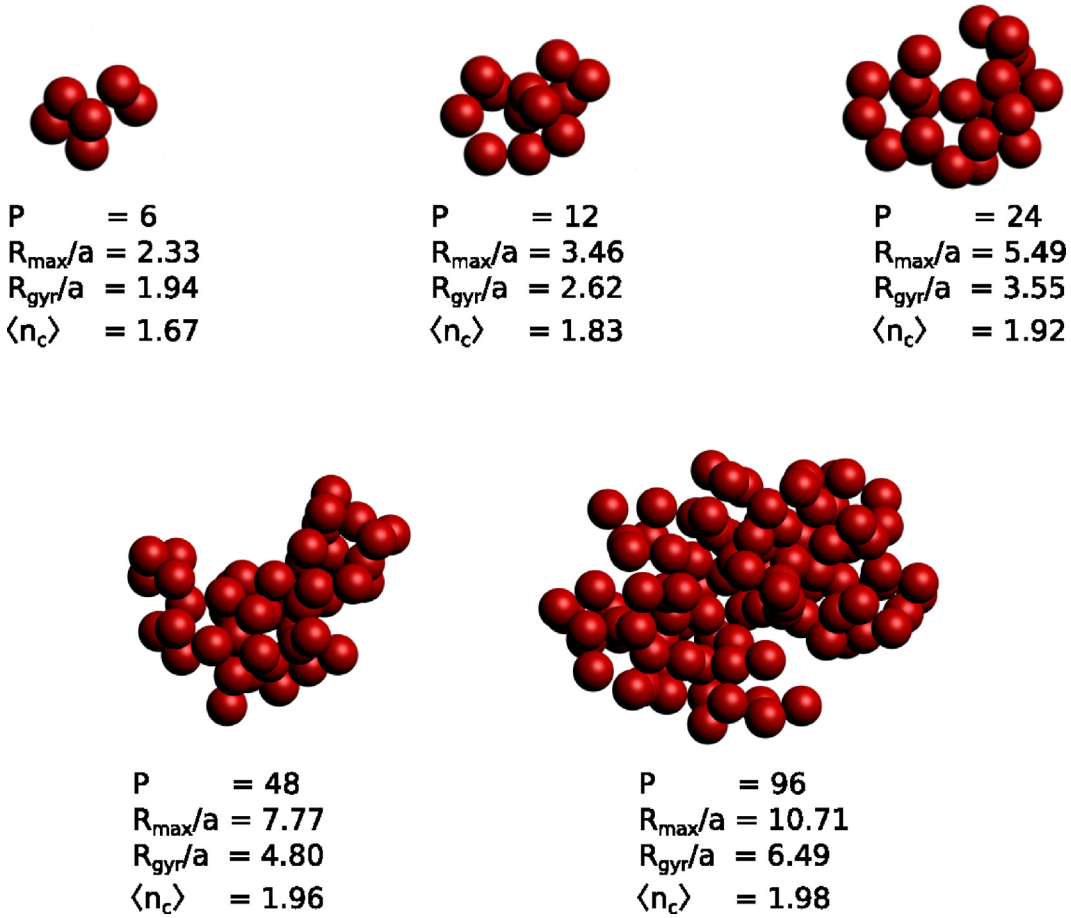

Fig. 5. A sample of the population of agglomerates used in the DEM simulations. Agglomerates are characterized according to the number of primary particles P, their outer radius R_{max}, their gyration radius R_g, and average coordination number $\langle n_c \rangle$. The primary particle radius a is 100 nm. All agglomerates have a fractal dimension d_f equal to 2.3.

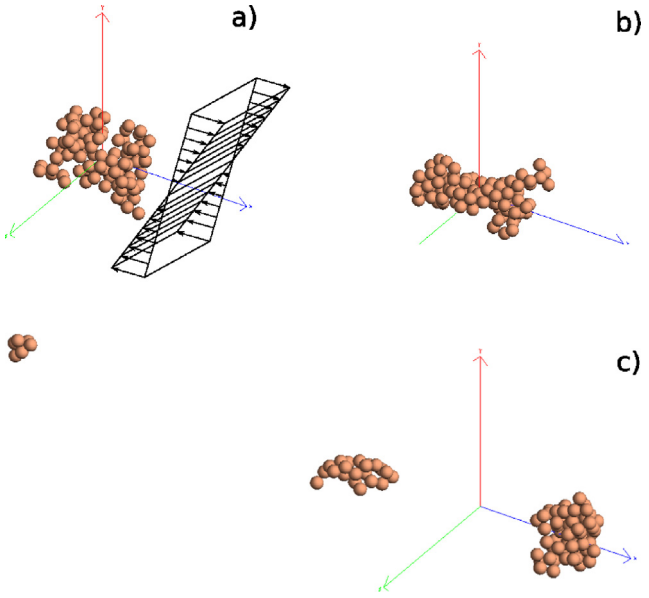

Fig. 6. Sequence of snapshots of a breakup event of an agglomerate subject to a ramp of increasing shear. (a) Initial morphology, (b) Restructured agglomerate, (c) Final fragments.

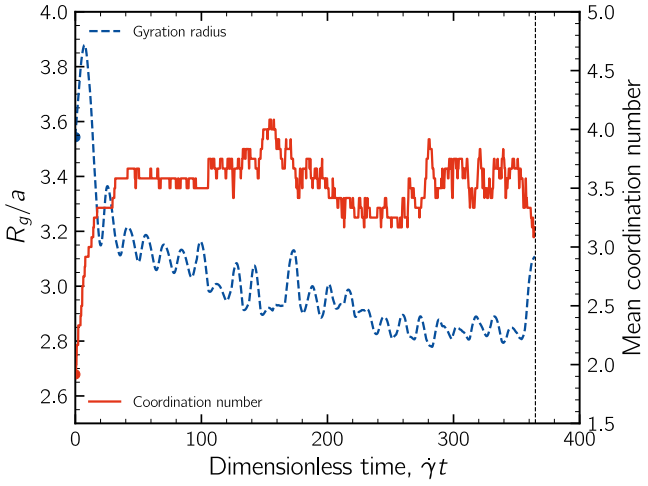

Fig. 7. Temporal evolution of the agglomerate gyration radius made dimensionless by the primary particle radius (left vertical axis) and average coordination number (right vertical axis). The vertical dotted line indicates the occurrence of the first breakup event. The shear stress varies linearly from 0 to 0.197 MPa.

the critical stress needed to induce breakup follow fairly well a power-law relationship with the initial gyration radius of the agglomerates, with a breakup exponent which only slightly changes among the three different data series, ranging between −0.75 and −1.0. In the inset of Fig. 8 the data have been made dimensionless by introducing a fragmentation dimensionless number defined as:

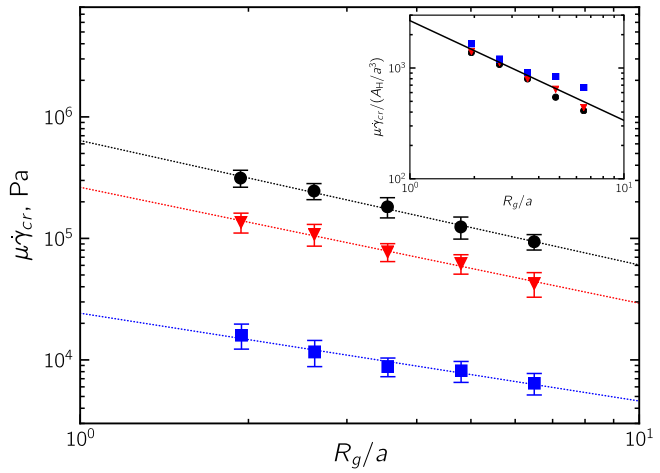

Fig. 8. Shear stress needed to break the agglomerates for different value of the particle–particle bond strength. Blue squares are for agglomerates for which A_H=0.966 · 10^{-20} J, for red triangles A_H=9.66 · 10^{-20} J, for black circles A_H=22.8 · 10^{-20} J. In the inset the data has made dimensionless by A_H/a^3.

$$Fr = \frac{\mu\dot{\gamma}_{cr}}{A_H/a^3} \tag{11}$$

which measures the ratio between the critical viscous stress $\mu\dot{\gamma}_{cr}$ and the characteristic bond strength A_H/a^3. It can been seen that the data collapse fairly well on a single master curve, with small deviations emerging only for the largest agglomerates. This makes it possible to conclude that the critical viscous stress data obtained in this work can be extended to count for the case of agglomerates characterized by a different bond strength intensity and/or size.

Besides the critical stresses, our DEM simulations returned the size and full morphology of the fragments generated upon breakup. In Fig. 9 we report the distribution of the size of the largest generated fragment, both after the first breakup event, and when the asymptotic fragment size distribution was reached. After the first breakup event (i.e. after the occurrence of the first bond failure which leads to the generation of two fragments) it can be noted that the maximum fragment has, in roughly the 80% of the cases, a mass which is about the 90% of the one of the parent agglomerate. However, the first breakup event is soon followed by a cascade of subsequent bond failures, and at equilibrium an

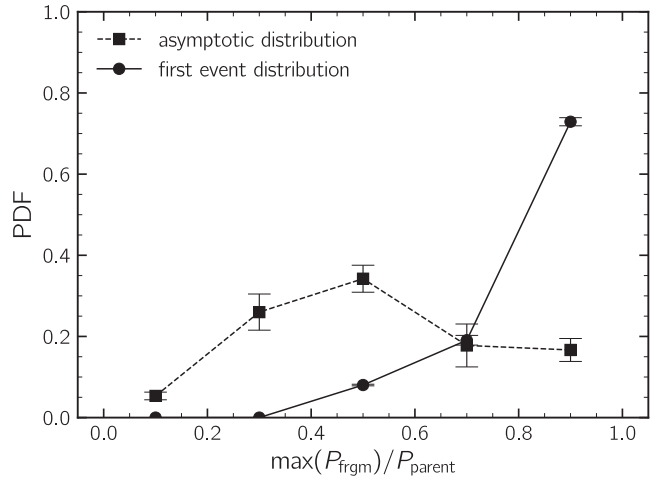

Fig. 9. Distribution of the size of the largest fragment generated after the first breakup event (circles) and at equilibrium (squares). Standard deviation bars indicate the deviations among data obtained at the different adopted values of the Hamaker constant. The PDF was calculated by dividing the abscissa in five classes of width 0.2.

average number of fragments typically ranging between two and six are generated, with the largest one which has in about the 40% of the cases a mass which is half the mass of the parent agglomerate. The case of a single breakup event leading to the formation of one large fragment shall also be expected (see the relatively large probability of having $\max(P_{frgm}/P_{parent})$ equal to 0.7 or 0.9 in the asymptotic size distribution). These results well compare with the ones reported in previous works where the agglomerate breakup was seen to lead to the formation of several fragments of scattered size (Eggersdorfer et al., 2010; Rwei et al., 1990).

3.3. Evaluation of breakup frequencies and population balance model calibration

The DEM and the CFD predictions have been combined and used to calibrate a simple population balance equation (PBE) model able to fully count for the breakup kinetics in the equipment.

In order to calculate the rate of fragmentation of the agglomerates, 1900 tracer particles were suspended in the flow and tracked according to the tracking algorithm described in Section 2.1. We applied first–passage–time statistics to the viscous stress time series so obtained and we measured the length of the time intervals τ_{brk} necessary for observing the first occurrence of a viscous stress strong enough to cause the failure of the agglomerate (Babler et al., 2012; De Bona et al., 2014): referring to Fig. 10 (top) and considering an agglomerate injected in the flow field at random time and space coordinates, the breakup time τ_{brk} was computed as the time the agglomerate takes to experience the condition $\mu\dot{\gamma} > \mu\dot{\gamma}_{cr}$, where $\mu\dot{\gamma}_{cr}$ is the critical stress determining its breakup. Breakup frequencies for varying critical stress were then computed as the inverse of the mean breakup time, obtained by averaging τ_{brk} over the trajectories of the 1900 tracer particles. The results of the first–passage–time statistics for the three different investigated flow fields are shown in Fig. 10 (bottom). As expected, breakup frequencies monotonously decrease as the agglomerates become more resistant. For all values of the power–law index of the fluid, two

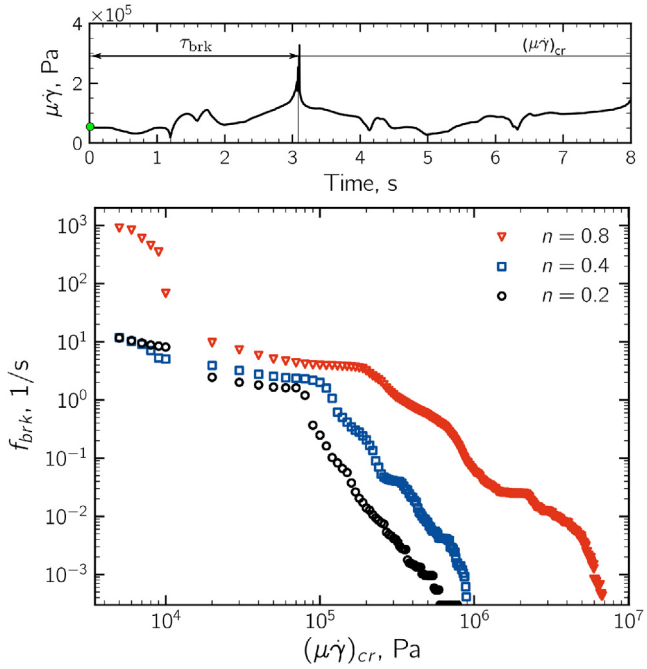

Fig. 10. Top) Illustration of the numerical procedure used to compute the breakup frequency for varying critical stress. Bottom) Breakup frequency as a function of the critical stress necessary for the agglomerate failure. Data were obtained by averaging the breakup times obtained by the analysis of 1900 shear stress signals.

regions of distinct slope can be identified in the graph, similarly to what was obtained for Newtonian systems (Frungieri et al., 2020b). For small values of $\mu\dot{\gamma}_{cr}$ (i.e., loose contacts and large agglomerates) the breakup frequency is large, and it mildly decreases. For small agglomerates and strong contacts (large $\mu\dot{\gamma}_{cr}$) the breakup frequency is lower and drops quite abruptly as $\mu\dot{\gamma}_{cr}$ grows. For the highest power–law index only ($n = 0.8$), there is a third region located at the smallest values of critical stresses, where the breakup frequency decreases rapidly of two orders of magnitude.

The plot of Fig. 10 can be seen as a kinetic law giving the rate of fragmentation in the equipment as a function of the agglomerate critical resistance $\mu\dot{\gamma}_{cr}$. This, coupled with the fragment size distribution reported in Fig. 9 and the critical viscous stress data obtained by the DEM simulations (Fig. 8), provides us with the information needed to setup a population balance model for the system, able to fully predict its dynamics.

Using a uniformly spaced grid for discretizing the agglomerate size interval, the population balance equations read as (Vanni, 2000):

$$\frac{dn_p}{dt} = b_p \qquad p = 1, 2, \ldots \tag{12}$$

where p is the number of primary particle composing the agglomerates, n_p is the number concentration of agglomerates made by a p number of primary particles and where b_p is the rate of agglomerate birth and death due to breakup. This has been modelled as:

$$b_p = -r_p^{(b)} + \sum_{q=p+1}^{\infty} \beta(p,q) r_q^{(b)} \tag{13}$$

where $r_p = n_p \cdot f_{brk}(p)$ is the rate of death of p-sized agglomerates due to breakup, and where the second term on the r.h.s. is the rate of birth of agglomerates composed by p particles, as a result of the breakup of the larger ones. We set the fragmentation rate term for each agglomerate class resorting to the power-law relating size and critical stress reported in Fig. 8 and by linearly interpolating the data reported in Fig. 10. The fragment size distribution β has been set according to the data obtained by the DEM simulations and reported in Fig. 9. However, we reduced the complexity of the asymptotic fragment size distribution to a ternary fragmentation mechanism, according to which breakup events result into a large fragment, which accounts for half the mass of the parent agglomerate, and in two other fragments whose mass is equal to a quarter of the mass of the parent agglomerate. The matrix $\beta(p,q)$ of Eq. (12) has been therefore set as:

$$\beta(p,4q) = \begin{cases} 1.0, & p = 2q \\ 2.0, & p = q \end{cases}$$

$$\beta(p,4q+1) = \begin{cases} 0.5, & p = 2q \\ 0.5, & p = 2q+1 \\ 1.5, & p = q \\ 0.5, & p = q+1 \end{cases}$$

$$\beta(p,4q+2) = \begin{cases} 0.5, & p = 2q+1 \\ 0.5, & p = 2q+2 \\ 1.5, & p = q \\ 0.5, & p = q+1 \end{cases} \tag{14}$$

$$\beta(p,4q+3) = \begin{cases} 0.5, & p = 2q+1 \\ 0.5, & p = 2q+2 \\ 0.5, & p = q \\ 1.5, & p = q+1 \end{cases}$$

$$q = 1, 2, 3, \ldots$$

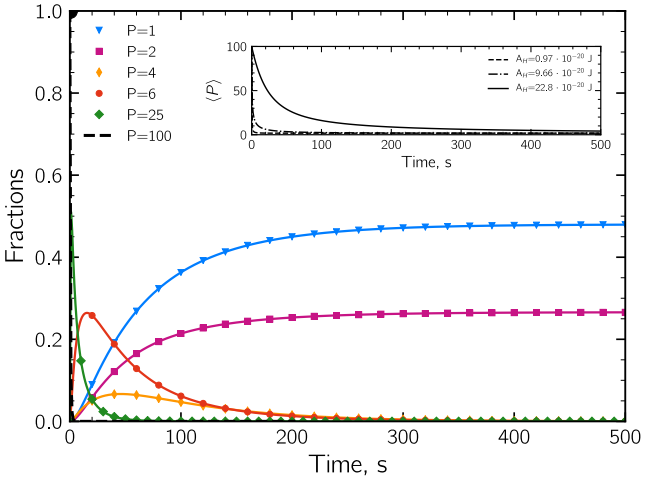

Fig. 11. Agglomerate number fraction for varying number of constituent primary particles. The black circle represents the population initial composition. In the inset the temporal evolution of the agglomerate average size is reported for three different particle–particle bond strength. Breakup frequencies for the $n = 0.2$ flow field of Fig. 10 were used to model the fragmentation rates.

Please notice that agglomerates composed by a number p of primary particles smaller than 4 have been assumed to be invulnerable to breakup, and so to be only generated, as a consequence of the breakup of the larger ones. The problem of Eq. (12) has been coded using Fortran and the time integration of the system of ordinary differential equations has been performed by the *lsode* solver of the library ODEPACK using the Adams–Moulton (AM) method for non-stiff problems. (Hindmarsh, 1983).

For the sake of conciseness, we limit ourselves to report the results of the breakup kinetics for the flow field of the power–law fluid with $n = 0.2$, and for an initially monodisperse population composed by agglomerates made by 100 primary particles, with $A_H = 9.66 \cdot 10^{-20}$ J. Fig. 11 reports the number concentration of a sample of agglomerate classes as a function of time, as obtained by the PBE model. It can be seen that the large agglomerates ($P = 100$) are rapidly broken down generating smaller agglomerates in the initial stage of the process. These, as can be seen from the $P = 25$ and $P = 6$ curves, are promptly produced in the initial stage of the process but their concentration approaches zero for large time as a consequence of their further breakup. At the asymptotic condition the population is made mostly by small agglomerates ($P < 4$) and large agglomerates are totally consumed. It is worth to notice that, due to the large variability of the breakup frequencies which span across several orders of magnitude with the agglomerate size, the average size of the agglomerate drops quite rapidly in the initial stage of the process, but the asymptotic size distribution is reached only at a later stage. Finally, in the inset, the effect of the particle–particle bond strength on the average size of the agglomerates is shown. As expected, as the agglomerates become looser (low A_H), the breakup dynamics is faster and the asymptotic average size is sooner reached. On the contrary, larger A_H values result into a slower breakup dynamics.

4. Conclusions

Herein, we presented the results of a numerical work aimed at investigating the dispersive mixing of solid filler agglomerates in a polymer compounding operation. The work uses computational fluid dynamics and discrete element method simulations, and finally combine data to calibrate a population balance model.

CFD simulations were run for three different values of the power–law index describing the shear-thinning behaviour of the fluid and returned the viscous stress distribution to which the agglomerates are subject to in the mixing equipment. Simulations made apparent that the power–law index has profound implications both on the flow field topology and typical viscous stress. DEM simulations, carried out to study the breakup behavior of the agglomerates, returned detailed insights into the breakup dynamics both in terms of critical shear stress for breakup and fragment size distribution. A power–law was found to fairly well describe the relationship between the critical stress and the size and strength of the agglomerates. Furthermore, the analysis of the fragment size distribution evolution showed that fragmentation occurs via a cascade of breakup events, resulting in a variable number of fragments, with the largest one often counting for the 50% of the mass of the parent agglomerate. A first–time passage–statistics conducted upon the shear stress time series experienced by the agglomerates allowed us to correlate the critical stress data with the equipment fluid dynamics and to compute the agglomerate breakup rates. Such data have been used finally to calibrate a population balance model which returned a full picture of the kinetics of the dispersive mixing process.

The work presented herein has been focused on the investigation of a polymer compounding mixing process. However, it is worth to point out that the methodology here reported can be easily adapted to investigate agglomerate breakup in different processes and flow fields, and data can be in the same way used to tune simple population balance models able to promptly predict fragmentation kinetics and particle size distribution for the process of interest.

Declaration of Competing Interest

The authors declare that they have no known competing financial interests or personal relationships that could have appeared to influence the work reported in this paper.

Acknowledgements

We gratefully acknowledge support from Prof. Daniele Marchisio and from the Virtual Material Marketplace project (www.vimmp.eu), within which the present work has been conducted. The project leading to this application has received funding from the European Union's Horizon 2020 research and innovation programme under grant agreement No 760907.

References

Babler, M.U., Biferale, L., Lanotte, A.S., 2012. Breakup of small aggregates driven by turbulent hydrodynamical stress. Phys. Rev. E 85, 025301. https://doi.org/10.1103/PhysRevE.85.025301.

Becker, V., Schlauch, E., Behr, M., Briesen, H., 2009. Restructuring of colloidal aggregates in shear flows and limitations of the free-draining approximation. J. Colloid Interface Sci. 339, 362–372. https://doi.org/10.1016/j.jcis.2009.07.022.

Berzin, F., Vergnes, B., Lafleur, P.G., Grmela, M., 2002. A theoretical approach to solid filler dispersion in a twin-screw extruder. Polym. Eng. Sci. 42, 473–481. https://doi.org/10.1002/pen.10964.

Blais, B., Vidal, D., Bertrand, F., Patience, G.S., Chaouki, J., 2019. Experimental methods in chemical engineering: Discrete element method-DEM. Can. J. Chem. Eng. 97, 1964–1973. https://doi.org/10.1002/cjce.23501.

Brady, J.F., Bossis, G., 1988. Stokesian dynamics. Annu. Rev. Fluid Mech. 20, 111–157. https://doi.org/10.1146/annurev.fl.20.010188.000551.

Breuer, M., Khalifa, A., 2019. Revisiting and improving models for the breakup of compact dry powder agglomerates in turbulent flows within Eulerian-Lagrangian simulations. Powder Technol. 348, 105–125. https://doi.org/10.1016/j.powtec.2019.03.009.

Cheng, J.-J., Manas-Zloczower, I., 1989. Hydrodynamic analysis of a Banbury mixer 2-D flow simulations for the entire mixing chamber. Polym. Eng. Sci. 29, 1059–1065. https://doi.org/10.1002/pen.760291512.

Cheng, J.-J., Manas-Zloczower, I., 1990. Flow field characterization in a Banbury mixer. Int. Polym. Process. 5, 178–183. https://doi.org/10.3139/217.900178.

Conchúir, B.O., Zaccone, A., 2013. Mechanism of flow-induced biomolecular and colloidal aggregate breakup. Phys. Rev. E 87, 032310. https://doi.org/10.1103/PhysRevE.87.032310.

Connelly, R.K., Kokini, J.L., 2006. Mixing simulation of a viscous Newtonian liquid in a twin sigma blade mixer. AIChE J. 52, 3383–3393. https://doi.org/10.1002/aic.10960.

De Bona, J., Lanotte, A.S., Vanni, M., 2014. Internal stresses and breakup of rigid isostatic aggregates in homogeneous and isotropic turbulence. J. Fluid Mech. 755, 365–396. https://doi.org/10.1017/jfm.2014.421.

Dhakal, P., Das, S.R., Poudyal, H., Chandy, A.J., 2017. Numerical simulations of partially-filled rubber mixing in a 2-wing rotor-equipped chamber. J. Appl. Polym. Sci. 134. https://doi.org/10.1002/app.44250.

Dominik, C., Tielens, A.G.G.M., 1997. The physics of dust coagulation and the structure of dust aggregates in space. Astrophys. J. 480, 647–673.

Durlofsky, L., Brady, J.F., Bossis, G., 1987. Dynamic simulation of hydrodynamically interacting particles. J. Fluid Mech. 180, 21–49. https://doi.org/10.1017/S002211208700171X.

Dutta, D., Ganda, A.N.F., Chih, J.-K., Huang, C.-C., Tseng, C.-J., Su, C.-Y., 2018. Revisiting graphene–polymer nanocomposite for enhancing anticorrosion performance: A new insight into interface chemistry and diffusion model. Nanoscale 10, 12612–12624. https://doi.org/10.1039/C8NR03261K.

Eckel, D.F., Balogh, M.P., Fasulo, P.D., Rodgers, W.R., 2004. Assessing organo-clay dispersion in polymer nanocomposites. J. Appl. Polym. Sci. 93, 1110–1117. https://doi.org/10.1002/app.20566.

Eggersdorfer, M.L., Kadau, D., Herrmann, H.J., Pratsinis, S.E., 2010. Fragmentation and restructuring of soft-agglomerates under shear. J. Colloid Interface Sci. 342, 261–268. https://doi.org/10.1016/j.jcis.2009.10.062.

Fanelli, M., Feke, D.L., Manas-Zloczower, I., 2006. Prediction of the dispersion of particle clusters in the nano-scale–Part I: Steady shearing responses. Chem. Eng. Sci. 61, 473–488. https://doi.org/10.1016/j.ces.2006.03.020.

Ferrás, L.L., Fernandes, C., Semyonov, D., Nóbrega, J.M., Covas, J.A., 2021. Dispersion of graphite nanoplates in polypropylene by melt mixing: The effects of hydrodynamic stresses and residence time. Polymers 13, 102. https://doi.org/10.3390/polym13010102.

Filippov, A.V., Zurita, M., Rosner, D.E., 2000. Fractal-like aggregates: Relation between morphology and physical properties. J. Colloid Interface Sci. 229, 261–273. https://doi.org/10.1006/jcis.2000.7027.

Freakley, P.K., Patel, S.R., 1987. Internal mixing: A practical investigation of the influence of intermeshing rotor configuration and operating variables on mixing characteristics and flow dynamics. Polym. Eng. Sci. 27, 1358–1370. https://doi.org/10.1002/pen.760271803.

Frungieri, G., Bäbler, M.U., Vanni, M., 2020a. Shear-induced heteroaggregation of oppositely charged colloidal particles. Langmuir 36, 10739–10749. https://doi.org/10.1021/acs.langmuir.0c01536.

Frungieri, G., Boccardo, G., Buffo, A., Marchisio, D., Karimi-Varzaneh, H.A., Vanni, M., 2020b. A CFD-DEM approach to study the breakup of fractal agglomerates in an internal mixer. Can. J. Chem. Eng. 98, 1880–1892. https://doi.org/10.1002/cjce.23773.

Frungieri, G., Vanni, M., 2017. Shear-induced aggregation of colloidal particles: A comparison between two different approaches to the modelling of colloidal interactions. Can. J. Chem. Eng. 95, 1768–1780. https://doi.org/10.1002/cjce.22843.

Frungieri, G., Vanni, M., 2021. Aggregation and breakup of colloidal particle aggregates in shear flow: A combined Monte Carlo-Stokesian dynamics approach. Powder Technol. 388, 357–370. https://doi.org/10.1016/j.powtec.2021.04.076.

Gastaldi, A., Vanni, M., 2011. The distribution of stresses in rigid fractal-like aggregates in a uniform flow field. J. Colloid Interface Sci. 357, 18–30. https://doi.org/10.1016/j.jcis.2011.01.080.

Gontarek, E., Macedonio, F., Militano, F., Giorno, L., Lieder, M., Politano, A., Drioli, E., Gugliuzza, A., 2019. Adsorption-assisted transport of water vapour in super-hydrophobic membranes filled with multilayer graphene platelets. Nanoscale 11, 11521–11529. https://doi.org/10.1039/C9NR02581B.

Gravelle, S., Kamal, C., Botto, L., 2020. Liquid exfoliation of multilayer graphene in sheared solvents: A molecular dynamics investigation. J. Chem. Phys. 152, 104701. https://doi.org/10.1063/1.5141515.

Hamaker, H.C., 1937. The London–van der Waals attraction between spherical particles. Physica 4, 1058–1072. https://doi.org/10.1016/S0031-8914(37)80203-7.

Harada, S., Tanaka, R., Nogami, H., Sawada, M., 2006. Dependence of fragmentation behavior of colloidal aggregates on their fractal structure. J. Colloid Interface Sci. 301, 123–129. https://doi.org/10.1016/j.jcis.2006.04.051.

Harshe, Y.M., Lattuada, M., 2012. Breakage rate of colloidal aggregates in shear flow through Stokesian dynamics. Langmuir 28, 283–292. https://doi.org/10.1021/la2038476.

Higashitani, K., Iimura, K., Sanda, H., 2001. Simulation of deformation and breakup of large aggregates in flows of viscous fluids. Chem. Eng. Sci. 56, 2927–2938. https://doi.org/10.1016/S0009-2509(00)00477-2.

Hindmarsh, A.C., 1983. ODEPACK: A systemized collection of ode solvers. Scientific computing, 55–64. URL https://computing.llnl.gov/projects/odepack/software.

Horwatt, S.W., Manas-Zloczower, I., Feke, D.L., 1992. Dispersion behavior of heterogeneous agglomerates at supercritical stresses. Chem. Eng. Sci. 47, 1849–1855. https://doi.org/10.1016/0009-2509(92)80303-T.

Manas-Zloczower, I., 2012. Mixing and compounding of polymers: Theory and practice. Carl Hanser Verlag, Munich, Germany.

Marchioli, C., Soldati, A., 2015. Turbulent breakage of ductile aggregates. Phys. Rev. E 91, 053003. https://doi.org/10.1103/PhysRevE.91.053003.

Marchisio, D.L., Vigil, R.D., Fox, R.O., 2003. Quadrature method of moments for aggregation–breakage processes. J. Colloid Interface Sci. 258, 322–334. https://doi.org/10.1016/S0021-9797(02)00054-1.

Marshall, J.S., 2009. Discrete-element modeling of particulate aerosol flows. J. Comput. Phys. 228, 1541–1561. https://doi.org/10.1016/j.jcp.2008.10.035.

Min, K., White, J.L., 1987. Flow visualization investigations of the addition of carbon black and oil to elastomers in an internal mixer. Rubber Chem. Technol. 60, 361–380. https://doi.org/10.5254/1.3536135.

Pantina, J.P., Furst, E.M., 2005. Elasticity and critical bending moment of model colloidal aggregates. Phys. Rev Lett. 94, 138301. https://doi.org/10.1103/PhysRevLett.94.138301.

Ren, Z., Harshe, Y.M., Lattuada, M., 2015. Influence of the potential well on the breakage rate of colloidal aggregates in simple shear and uniaxial extensional flows. Langmuir 31, 5712–5721. https://doi.org/10.1021/la504966y.

Rwei, S.-P., Manas-Zloczower, I., Feke, D.L., 1990. Observation of carbon black agglomerate dispersion in simple shear flows. Polym. Eng. Sci. 30, 701–706. https://doi.org/10.3139/217.910098.

Salahudeen, S.A., Elleithy, R.H., AlOthman, O., AlZahrani, S.M., 2011. Comparative study of internal batch mixer such as cam, Banbury and roller: Numerical simulation and experimental verification. Chem. Eng. Sci. 66, 2502–2511. https://doi.org/10.1016/j.ces.2011.02.017.

Saxena, A., Kroll-Rabotin, J.-S., Sanders, R.S., 2022. Numerical investigation of the respective roles of cohesive and hydrodynamic forces in aggregate restructuring under shear flow. J. Colloid Interface Sci. 608, 355–365. https://doi.org/10.1016/j.jcis.2021.08.208.

Seto, R., Botet, R., Briesen, H., 2011. Hydrodynamic stress on small colloidal aggregates in shear flow using Stokesian dynamics. Phys. Rev. E 84, 041405. https://doi.org/10.1103/PhysRevE.84.041405.

Shah, K.J., Shukla, A.D., Shah, D.O., Imae, T., 2016. Effect of organic modifiers on dispersion of organoclay in polymer nanocomposites to improve mechanical properties. Polymer 97, 525–532. https://doi.org/10.1016/j.polymer.2016.05.066.

Tang, B., Hu, G., Gao, H., Hai, L., 2015. Application of graphene as filler to improve thermal transport property of epoxy resin for thermal interface materials. Int. J. Heat Mass Transfer 85, 420–429. https://doi.org/10.1016/j.ijheatmasstransfer.2015.01.141.

Thacker, W.I., Zhang, J., Watson, L.T., Birch, J.B., Iyer, M.A., Berry, M.W., 2010. Algorithm 905: SHEPPACK: Modified Shepard algorithm for interpolation of scattered multivariate data. ACM Trans. Math. Softw. 37, 1–20. https://doi.org/10.1145/1824801.1824812.

Thouy, R., Jullien, R., 1994. A cluster-cluster aggregation model with tunable fractal dimension. J. Phys. A: Math. Gen 27, 2953. https://doi.org/10.1088/0305-4470/27/9/012.

Turetta, L., Lattuada, M., 2022a. Brownian dynamics simulations of shear-induced aggregation of charged colloidal particles in the presence of hydrodynamic interactions. J. Colloid Interface Sci. 624, 637–649. https://doi.org/10.1016/j.jcis.2022.05.047.

Turetta, L., Lattuada, M., 2022b. The role of hydrodynamic interactions on the aggregation kinetics of sedimenting colloidal particles. Soft Matter 18, 1715–1730.

Vanni, M., 2000. Approximate population balance equations for aggregation–breakage processes. J. Colloid Interface Sci 221, 143–160. https://doi.org/10.1006/jcis.1999.6571.

Vanni, M., 2015. Accurate modelling of flow induced stresses in rigid colloidal aggregates. Comput. Phys. Commun. 192, 70–90. https://doi.org/10.1016/j.cpc.2015.02.022.

Vanni, M., Gastaldi, A., 2011. Hydrodynamic forces and critical stresses in low-density aggregates under shear flow. Langmuir 27, 12822–12833. https://doi.org/10.1021/la2024549.

Vasquez Giuliano, L., Buffo, A., Vanni, M., Lanotte, A.S., Arima, V., Bianco, M., Baldassarre, F., & Frungieri, G. (2022). Response of shear-activated nanotherapeutic particles in a clot-obstructed blood vessel by CFD-DEM simulations. Can. J. Chem. Eng., in press. doi:10.1002/cjce.24502.

Yang, H.-H., Manas-Zloczower, I., 1992. 3D flow field analysis of a Banbury mixer. Int. Polym. Process. 7, 195–203. https://doi.org/10.3139/217.920195.

Zaccone, A., Soos, M., Lattuada, M., Wu, H., Bäbler, M.U., Morbidelli, M., 2009. Breakup of dense colloidal aggregates under hydrodynamic stresses. Phys. Rev. E 79, 061401. https://doi.org/10.1103/PhysRevE.79.061401.